Synthesis of Petal-Like MnO$_2$ Nanosheets on Hollow Fe$_3$O$_4$ Nanospheres for Heterogeneous Photocatalysis of Biotreated Papermaking Effluent

Yangliu Du [1,2], Fuqiang Li [1,2], Yecan Peng [1,2], Shaowu Jia [1,2], Lei Lan [1,2], Jinghong Zhou [1,2,*] and Shuangfei Wang [1,2]

[1] School of Light Industry and Food Engineering, Guangxi University, Nanning 530004, China
[2] Guangxi Key Laboratory of Clean Pulp & Papermaking and Pollution Control, Nanning 530004, China
* Correspondence: jhzhoudou@gxu.edu.cn; Tel.: +86-134-7100-2595

check for
updates

Abstract: Owing to the implementation of increasingly stringent water conservation policies and regulations, the pulp and paper mill industry must make increased efforts to meet the limits for pollutant emissions. The primary pretreatment and secondary biochemical treatment methods used currently generally fail to meet the country-specific environmental regulations, and the wastewater must be processed further even after being subjected to secondary biochemical treatments. In this work, we synthesized Fe$_3$O$_4$/MnO$_2$ nanocomposites (FMNs) with a flower-like structure for use in the heterogeneous photocatalytic treatment of biotreated papermaking wastewater. FMNs1.25, which were formed using a KMnO$_4$/Fe$_3$O$_4$ molar ratio of 1.25, could be separated readily using an external magnetic field and exhibited higher photocatalytic activity than those of the other samples as well as MnO$_2$ and Fe$_3$O$_4$. The effects of various experimental parameters on the photocatalytic activity of FMNs1.25, including the initial pH of the wastewater and the catalyst dosage, were determined. The common chemical oxygen demand (COD$_{Cr}$) reduction rate in the case of this sample reached 56.58% within 120 min at a pH of 3, the COD$_{Cr}$ of effluent after treatment was 52.10 mg/L. Further, even under neutral conditions, the COD$_{Cr}$ of the treated effluent was below the current limit for discharge in China. Moreover, the nanocomposites exhibited good recyclability, and their catalytic activity did not decrease significantly even after five usage cycles. This study should serve as a platform for the fabrication of effective photocatalysts for the advanced treatment of biotreated papermaking effluent and refractory organic wastewater.

Keywords: Fe$_3$O$_4$/MnO$_2$ nanocomposites; magnetic catalyst; photocatalysis; advanced treatment; bio-treated effluent of papermaking

1. Introduction

The effective treatment of wastewater plays an important role in maintaining the ecological balance of the natural environment [1–7]. Pulp and paper mills consume a lot of water and, at the same time, emit a considerable amount of wastewater [8,9]. Primary pretreatments and secondary biochemical treatments are the main steps in wastewater treatment [10,11]. Owing to the problems related to the scale, papermaking materials and bleaching methods used, wastewater recycling rate, wastewater treatment technology employed, and equipment renewal, some pollutants inevitably remain in the final discharged wastewater. In China, because of the increasingly strict environmental protection guidelines and the implementation of stricter regulations, it has become essential to subject wastewater to additional treatments. However, these advanced treatments for wastewater pose an urgent problem in case of the pulp and paper industry [12]. It is very important to remove the organic pollutants

present in pulp and papermaking wastewater, as these compounds are refractory, toxic, mutative, and carcinogenic and can have long-term harmful effects on the ecological environment [13]. Photocatalytic oxidation techniques have many advantages. For instance, they involve mild and controllable reaction conditions, allow for the oxidative degradation of organic matter, and do not result in the secondary pollution of the environment. As a result, they are being studied widely [14–16].

MnO_2, a typical transition metal oxide, is used extensively in batteries [17–19], supercapacitors [20–22], and photocatalysts [23–27] because of its special physical and chemical properties. Moreover, C_3N_4/MnO_2 nanocomposites have been synthesized and used for the photocatalytic degradation of phenol and dye during water treatment [28]. Further, films of CuO/MnO_2 nanorod arrays have been synthesized and used for the efficient catalytic oxidation of acid fuchsin dye [29]. Similarly, mesoporous MnO_2 has been fabricated and utilized in the catalytic ozonation of 4-nitrophenol [30] while hierarchically structured $MnO_2@SiO_2$ nanofibrous membranes have been employed for the degradation of methylene blue [31]. These studies have shown that MnO_2 has wide applicability as an efficient catalytic material. Nevertheless, MnO_2 alone or nonmagnetic MnO_2-containing heterogeneous catalysts cannot be separated and recycled readily after the treatment reaction. This increases the cost associated with their industrial use and also causes additional pollution [32]. Therefore, the development of novel catalysts with high separability and recyclability is essential. The magnetic separation technique provides a practical solution to this problem [33]. Loading MnO_2 nanosheets onto the surfaces of Fe_3O_4 nanoparticles is an easy way of producing nanocomposite catalysts that can be removed and recycled readily using an external magnetic field. The durability of these catalysts is also high [34,35]. Zhang et al. [27] prepared a magnetic recyclable thin-layer MnO_2 coated Fe_3O_4 nanocomposite by hydrothermal method combined with a mild ultrasonic means and used it in the photocatalytic decolorization of model pollutant MB (methylene blue) under ultraviolet irradiation. The results showed that the maximum photodegradation rate was 98.2% after UV-vis light irradiation for 3h. However, few studies have been done on the treatment of industrial wastewater by MnO_2/Fe_3O_4 nanocomposite, especially in the advanced treatment of the biotreated effluent of papermaking wastewater, which has a complex composition, containing lignin, hemicellulose, residual alkali, sugars, inorganic salts, volatile acids, organic chlorides, etc.

In this study, hollow Fe_3O_4 nanospheres (HFNs) and flower-like Fe_3O_4/MnO_2 nanocomposites (FMNs) based on these HFNs were synthesized through a simple process. First, the HFNs were fabricated through a hydrothermal method using different initial $(NH_2)_2CO/C_6H_5Na_3O_7·2H_2O$ molar ratios. Next, the FMNs were fabricated via the coprecipitation method using different $KMnO_4/Fe_3O_4$ molar ratios. The fabricated HFNs had a raspberry-like surface, which allowed for a high catalyst surface area as well as the ready growth of the MnO_2 nanosheets. The synthesized FMNs were subsequently used for the treatment of the biotreated effluent of papermaking wastewater. The effects of the molar ratios of the reactants on the morphologies of the HFNs and FMNs were evaluated. In addition, the effects of several other factors on the efficiency of the heterogeneous photocatalytic reaction were also studied in detail. Finally, the decrease in the common chemical oxygen demand (COD_{Cr}) after the heterogeneous photocatalysis process and the recyclabilities of the photocatalysts were also investigated.

2. Materials and Methods

2.1. Materials Used

Ferric chloride hexahydrate ($FeCl_3·6H_2O$), potassium permanganate ($KMnO_4$), and urea ($(NH_2)_2CO$) were purchased from Guangdong Guanghua Sci-Tech Co. Ltd (Guangzhou, China). Sodium citrate ($C_6H_5Na_3O_7·2H_2O$), sulfuric acid (H_2SO_4, 95%–98%), fuming hydrochloric acid (HCl, 37%), and ethanol (CH_3CH_2OH, ≥99.7%) were purchased from Tianjin Zhiyuan Chemical Co. Ltd. (Tianjin, China). Polyacrylic acid (30% solid, average M_w: 3000) was purchased from Shanghai Macklin Biochemical Co. Ltd (Shanghai, China). All the reagents were analytical grade. Deionized water with

a resistivity of 18.0 MΩ·cm^{-1} was obtained from a Milli-Q apparatus (Millipore, Bedford, MA, USA) and was used throughout the study. The wastewater used was the biotreated effluent from a factory of the Guangye Guitang Sugar Group Co., Ltd (Guigang, China). The pH of the wastewater was 6.58 and its COD_{Cr} was 120 mg·L^{-1}.

2.2. Synthesis of Hollow Fe$_3$O$_4$ Nanospheres (HFNs)

The HFNs were synthesized by the conventional hydrothermal method [27], different reactant molar ratios were used in the synthesis experiment. First, 4 mmol of $FeCl_3·6H_2O$, different amounts (16, 18, and 20 mmol) of $(NH_2)_2CO$, and different amounts (8 and 12 mmol) of $C_6H_5Na_3O_7·2H_2O$ were dissolved in 60 mL of deionized water and stirred continuously for 30 min at room temperature. Then, 0.75 mL of polyacrylic acid was added to the resulting dispersion. After being constantly stirred for 30 min, the mixture was transferred to a 100 mL Teflon-lined autoclave and kept at 200 °C for 12 h. Next, the autoclave was cooled to room temperature, the products were washed with deionized water and ethanol three times, and finally dried at 60 °C in a vacuum oven. The HFN samples obtained were labeled as HFNs1, HFNs2, HFNs3, HFNs4, HFNs5, and HFNs6. The experimental parameters used to fabricate these samples are listed in Table 1.

Table 1. Experimental parameters used for synthesis of hollow Fe$_3$O$_4$ nanospheres (HFNs).

Sample	FeCl$_3$·6H$_2$O (mmol)	(NH$_2$)$_2$CO (mmol)	C$_6$H$_5$Na$_3$O$_7$·2H$_2$O (mmol)	PAA (mL)	H$_2$O (mL)
HFNs1	4	16	8	0.75	60
HFNs2	4	18	8	0.75	60
HFNs3	4	20	8	0.75	60
HFNs4	4	16	12	0.75	60
HFNs5	4	18	12	0.75	60
HFNs6	4	20	12	0.75	60

2.3. Synthesis of Fe$_3$O$_4$/MnO$_2$ Nanocomposites (FMNs)

The FMNs were synthesized through a modified coprecipitation process. First, $KMnO_4$ (0.75, 1.5, 1.875, 2.25, or 3 mmol) was dissolved in 75 mL of deionized water. Then, 1 mL of fuming hydrochloric acid was added to the solution in a dropwise manner. After the mixture had been stirred for 30 min, 1.5 mmol of the as-prepared HFNs was dispersed evenly in the solution. Next, the mixture was stirred for 30 min at room temperature and heated to 90 °C and kept at that temperature for 90 °C for 3 h. The obtained brownish-black product was sequentially washed with deionized water and ethanol. Finally, the product was dried at 60 °C for 24 h in a vacuum oven. The synthesized FMN samples were labeled as FMNs0.5, FMNs1, FMNs1.25, FMNs1.5, and FMNs2, and the experimental parameters used to produce them are listed in Table 2.

Table 2. Experimental parameters used for synthesis of Fe$_3$O$_4$/MnO$_2$ nanocomposites (FMNs).

Sample	KMnO$_4$ (mmol)	Fe$_3$O$_4$ (mmol)	HCl (mL)	H$_2$O (mL)
FMNs0.5	0.75	1.5	1	75
FMNs1	1.5	1.5	1	75
FMNs1.25	1.875	1.5	1	75
FMNs1.5	2.25	1.5	1	75
FMNs2	3	1.5	1	75

2.4. Characterization

The X-ray diffraction (XRD) patterns of the FMNs were acquired using a Rigaku MiniFlex600 X-ray diffractometer (Rigaku, Tokyo, Japan) with a Cu-Kα radiation source. The measurements were performed at 40 kV × 15 mA and 2θ values of 5–80°. X-ray photoelectron spectroscopy (XPS)

was used to determine the surface chemical compositions of the samples. The XPS analyses were performed using a Thermo ESCALAB 250XI spectrometer (Thermo Scientific, Waltham, MA, USA) with an Al-Kα radiation source. The C1s peak at 284.6 eV was used as the internal reference peak for calibration. Fourier transform infrared spectroscopy (FT-IR, Bruker Tensor II, Bruker, Karlsruhe, Germany) was also performed on the samples; KBr was used to form the tablets for the measurements. The surface morphologies of the samples were characterized using a ZEISS SIGMA HD field-emission scanning electron microscopy (FESEM) system (Zeiss, Oberkochen, Germany) and a FEI Tecnai G2 F20 transmission electron microscopy (TEM) system (FEI, Hillsboro, OR, USA). An LDJ 9600 vibrating sample magnetometer (LDJ Electronics, Dayton, OH, USA) was used to determine the magnetic properties of the as-prepared samples. The Brunauer–Emmett–Teller (BET) surface areas ($m^2\ g^{-1}$) of the samples were measured at 77 K using a Micromeritics TriStar II 3flex automatic specific surface and porosity analyzer (Micromeritics Instruments Corporation, Norcross, GA, USA). The zeta potential of the suspension was recorded on a Malvern Panalytical NANO ZS90 (Malvern Ltd, Malvern, UK). The 3D-excitation-emission-matrix (3D-EEM) spectra of the treated wastewater samples were obtained using a Horiba FluoroMax-4 fluorescence spectrophotometer (Horiba, Kyoto, Japan). The excitation wavelengths were 220–440 nm, while the emission wavelengths were 300–600 nm. The COD_{Cr} values of the treated wastewater samples were measured using a COD/ammonia nitrogen double-parameter rapid tester (5B-3C(V8), Beijing Lianhua Technology Co. Ltd, Beijing, China).

2.5. Heterogeneous Photocatalytic Tests

The heterogeneous photocatalytic treatment of the secondary biotreated effluent of pulp and paper mill wastewater was performed in a GHX-V photochemical reactor (Shanghai Jiapeng Technology Co., Ltd., Shanghai, China); a schematic of the device is shown in Figure 1. The light source used was a 200 W high-pressure mercury lamp (wavelengths of 350–450 nm), and the reaction temperature was adjusted to 25 ± 2 °C. During each run, 250 mL of the wastewater was added to the reactor, and the initial pH of the reaction was adjusted using a 0.1 M NaOH or H_2SO_4 solution. Next, a certain amount of the FMNs sample in question was added to the solution. The suspension was stirred continuously and exposed to light. The COD_{Cr} value was determined by taking water samples at regular intervals. All the experiments were performed for same duration (180 min) in order to elucidate the effects of the photocatalytic treatment. Each group of samples was tested thrice, and the average COD_{Cr} was calculated. The COD_{Cr} removal rate of wastewater (α) can be calculated from the initial COD_{Cr} (C_0) and the COD_{Cr} during sampling (C_t) as follows:

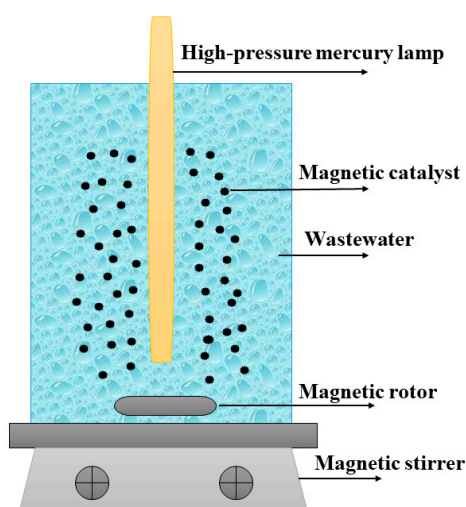$$\alpha = (C_0 - C_t)/C_0 \times 100\% \tag{1}$$

Figure 1. Schematic of reactor used for heterogeneous photocatalytic reaction.

3. Results and Discussion

3.1. Characterization of Hollow Fe₃O₄ Nanospheres and Fe₃O₄/MnO₂ Nanocomposites

Figure 2a shows the XRD patterns of FMNs0.5, HFNs1, HFNs1.25, HFNs1.5, and HFNs2. The diffraction peaks at 2θ of 30.08°, 35.43°, 37. 02°, 43.08°, 53.42°, 56.95°, and 62.68° correspond to the (220), (311), (222), (400), (422), (511), and (440) reflection planes, respectively, and are consistent with the standard pattern of magnetite Fe_3O_4 (JCPDS Card No. 19-0629). Further, the diffraction peak appearing at 2θ of 65.98° is in keeping with the standard spectrum of γ-MnO_2 (JCPDS Card No. 12–0714) and corresponds to MnO_2 [36–38].
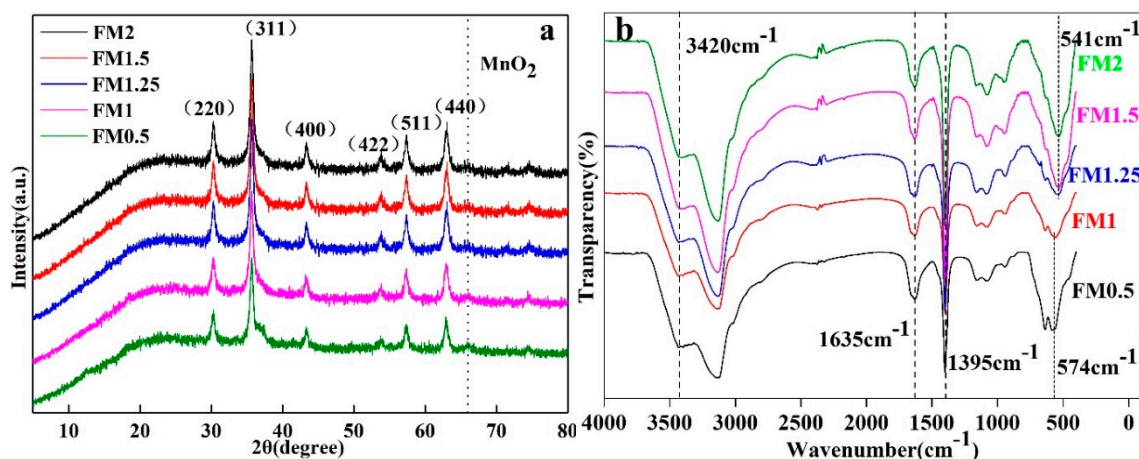
Figure 2. (**a**) XRD patterns and (**b**) FT-IR spectra of synthesized FMNs.

The FTIR spectra of the as-synthesized nanocomposites are shown in Figure 2b. In the cases of FMNs0.5 and FMNs1, the absorption peak at 574 cm^{-1} can be assigned to the Fe-O stretching vibrations that occur in iron oxide. Further, the characteristic peak at 3420 cm^{-1} is related to the stretching vibrations of the O-H bond and may be ascribable to the hydroxyl groups present on the sample surfaces. The peak at 1635 cm^{-1} corresponds to COO-stretching in citrates or peroxyacetic acid, while the peak at 1395 cm^{-1} can be attributed to the stretching of the C-O bond in citrates [39]. The peak at 458 cm^{-1} can be ascribed to the stretching of the Mn-O bond in MnO_2 [40]. In addition, a peak related to the Fe-O stretching vibrations was also observed in the cases of FMNs1.25, FMNs1.5, and FMNs2 but at a lower wavenumber (541 cm^{-1}), owing to an increase in the Mn-O bond strength [41].

The chemical compositions and oxide states of the FMN samples were studied by XPS. The integral survey spectrum of FMNs1.25 is displayed in Figure 3a, which shows the binding energies of the Fe(2p), Mn(2p), O(1s), and C(1s) peaks of the nanocomposite. Figure 3b shows that two high-intensity bands with binding energies of 711.1 and 724.9 eV were present; these were the Fe2p$_{3/2}$ and Fe2p$_{1/2}$ peaks, respectively, and corresponded to the Fe^{2+} (FeO) and Fe^{3+} (Fe_2O_3) states, respectively, of Fe and were characteristic of the Fe_3O_4 structure [38–40]. Further, as can be seen from Figure 3c, the binding energies of the Mn2p$_{3/2}$ and Mn2p$_{1/2}$ peaks were 642.5 and 654.1 eV, respectively, indicating the presence of Mn^{4+} in the sample. These results were in keeping with previous reports [40,42]. Hence, these characterization data confirmed that the FMNs had been synthesized successfully.
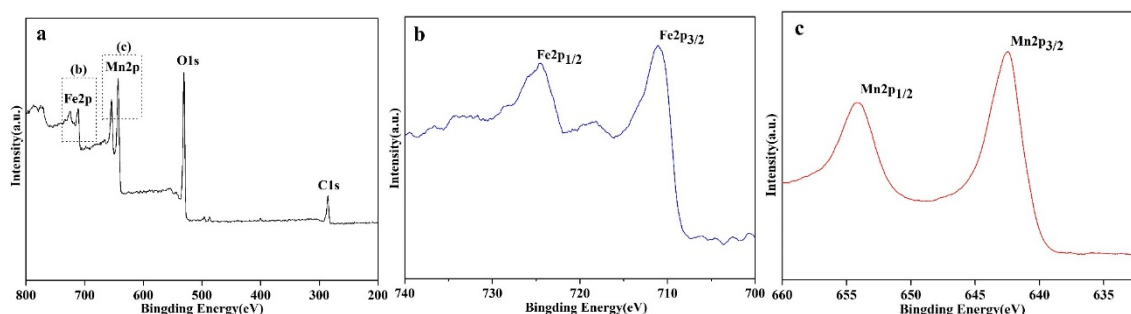
Figure 3. XPS survey spectrum of (**a**) FMNs1.25 and corresponding high-resolution (**b**) Fe2p, and (**c**) Mn2p spectra.

The dosages of $(NH_2)_2CO$ and $C_6H_5Na_3O_7 \cdot 2H_2O$ determined both the morphology and the size of the HFNs. Figure 4 shows FESEM images of the HFNs synthesized using the different initial $(NH_2)_2CO/C_6H_5Na_3O_7 \cdot 2H_2O$ molar ratios. Figure 4a–c show the images of the HFNs produced using 8 mmol of $C_6H_5Na_3O_7 \cdot 2H_2O$. It can be seen from Figure 4a that the nanoparticles of sample HFNs1 had diameters of 20–30 nm. With an increase in the amount of $(NH_2)_2CO$ added, as shown in Figure 4b,c, nanoparticles with rough surfaces and a diameter of approximately 200 nm were formed, as in the cases of HFNs2 and HFNs3. Moreover, a few incompletely formed spherical structures were also observed, indicating that the formed nanospheres were hollow. Figure 4d–f show FESEM images of the HFNs formed using 12 mmol of $C_6H_5Na_3O_7 \cdot 2H_2O$. It can be seen clearly that the HFNs had diameters of 200–300 nm and were well dispersed and fully formed. In summary, it can be concluded that the amount of $C_6H_5Na_3O_7 \cdot 2H_2O$ used had a determining effect on the morphology and size of the HFNs formed. According to the molding conditions of the hollow nanospheres, HFNs6 sample was selected as the raw material for the subsequent experiments.
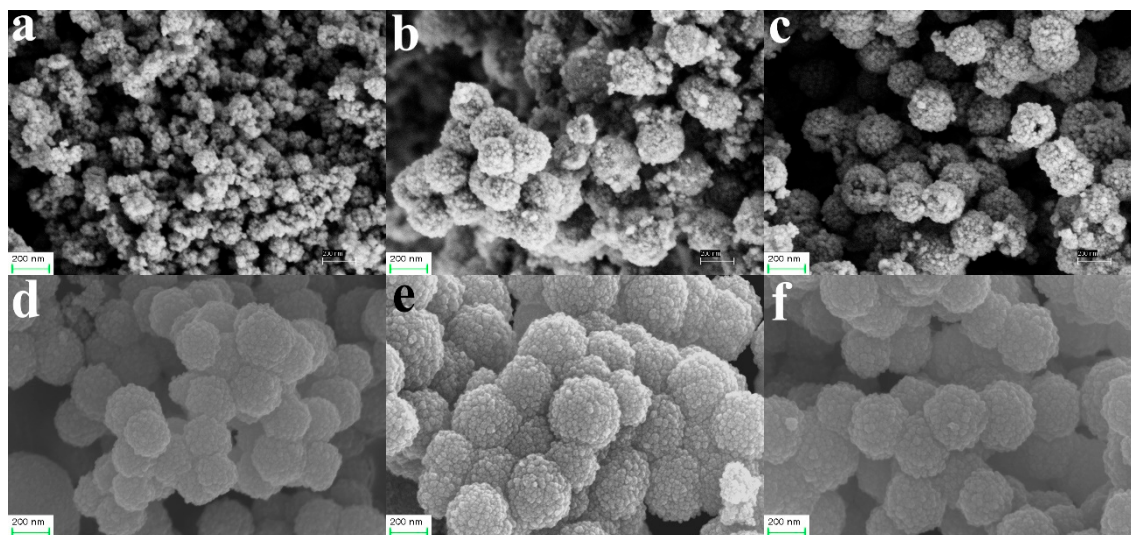

Figure 4. Field-emission scanning electron microscopy (FESEM) images of (**a**) HFNs1, (**b**) HFNs2, (**c**) HFNs3, (**d**) HFNs4, (**e**) HFNs5, and (**f**) HFNs6.

Next, the as-synthesized HFNs6 sample and different amounts of $KMnO_4$ were used to prepare the various FMN samples by the coprecipitation method. The morphologies and microstructures of the fabricated FMNs can be seen from the FESEM and TEM images shown in Figures 5 and 6, respectively. Figure 5 shows that, with an increase in the amount of $KMnO_4$ added, the growth of the MnO_2 nanosheets on the surfaces of the HFNs also increased. When the $KMnO_4/Fe_3O_4$ molar ratio was increased to two, the MnO_2 nanosheets turned into petal-like structures and completely covered

the HFNs. This confirmed indirectly that the degree of bonding between the MnO_2 nanosheets and the HFNs was high, resulting in well-structured nanocomposites.
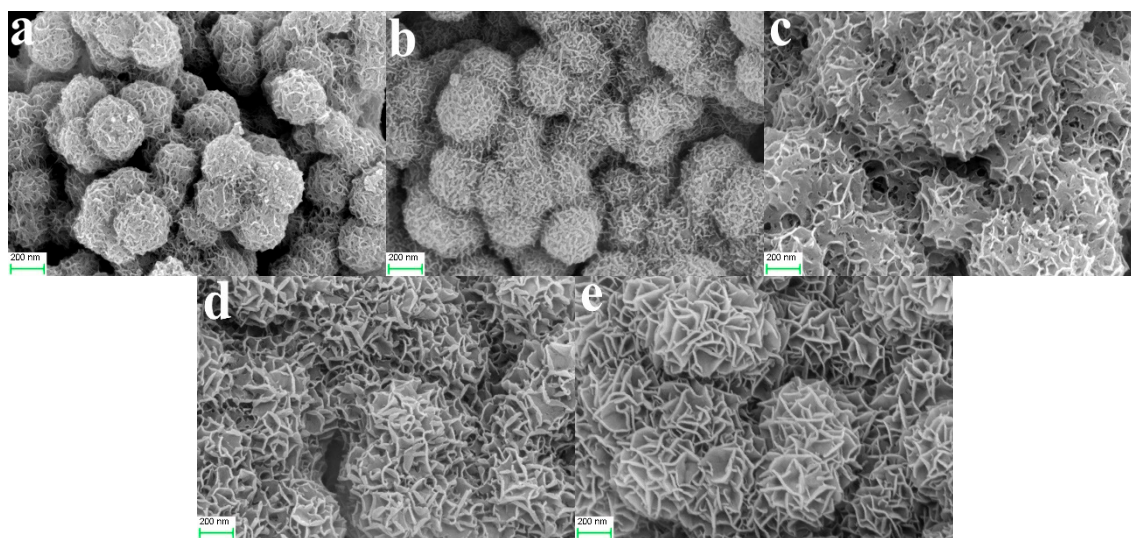

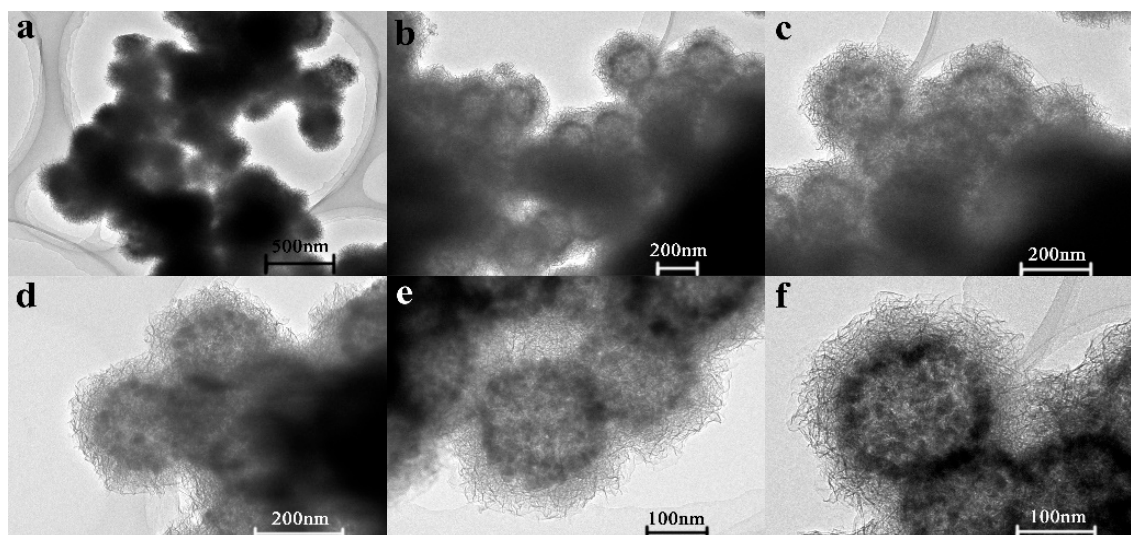**Figure 5.** FESEM images of (**a**) FMNs0.5, (**b**) FMNs1, (**c**) FMNs1.25, (**d**) FMNs1.5, and (**e**) FMNs2.

Figure 6. Transmission electron microscopy (TEM) images of FMNs1.25 at (**a**) 10,000×, (**b**) 15,000×, (**c**) 25,000×, (**d**) 30,000×, (**e**) 40,000× and (**f**) 50,000× magnification.

The TEM images (Figure 6) also showed that FMNs1.25 consisted of nanospheres whose surfaces were completely coated with nanosheets. It can be seen from Figure 6b–e that the nanospheres had a black edge and a grayish-white central region. This confirmed that they were hollow.

The BET surface areas and pore characteristics of HFNs6 and the various FMNs are presented in Figure 7a. The BET surface area of pure Fe_3O_4 (HFNs6) was 63.69 m^2/g, much lower than the value of MnO_2 nanosheet. Further, with an increase in the loading rate of MnO_2, the BET surface area of the nanocomposites (from FMNs0.5 to FMNs1.25) increased from 201.76 m^2/g to 214.36 m^2/g, much higher than the values of pure Fe_3O_4 due to the amount of MnO_2 nanosheet. FMNs1.25 had the largest BET surface area at 214.36 m^2/g. However, when the $KMnO_4/Fe_3O_4$ molar ratio was increased to two, the BET surface area of FMNs2, was low at 192.00 m^2/g, suggesting that excess $KMnO_4$ solution could not increase the BET. The trend in the Barrett–Joyner–Halenda (BJH) pore volume of the

nanocomposites was the same as that in the BET surface area, with FMNs1.25 exhibiting the highest BJH pore volume at 0.45 cm^3/g.

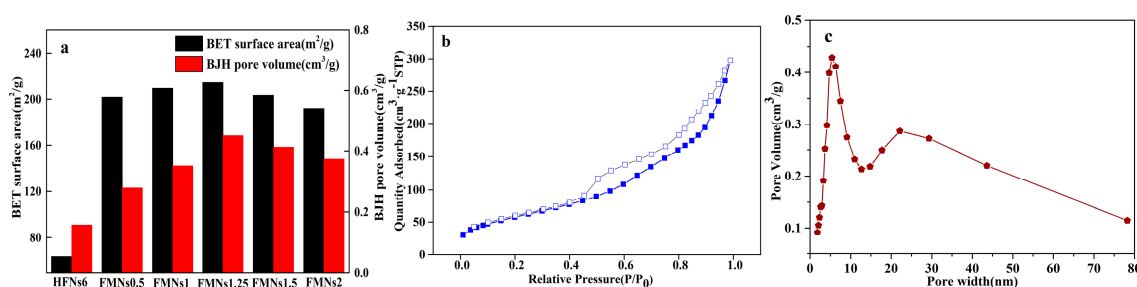**Figure 7.** (**a**) Brunauer–Emmett–Teller (BET) surface areas and pore characteristics of HFNs6 and synthesized FMNs and (**b**) N$_2$ adsorption–desorption isotherm and (**c**) pore size distribution of FMNs1.25.

The N$_2$ adsorption–desorption isotherm of FMNs1.25 and its pore size distribution are shown in Figure 7b,c. There is significant hysteresis between the adsorption and desorption arms of the isotherm for P/P$_0$ values between 0.4 and 1.0 (see Figure 7b); this was indicative of a typical mesoporous structure [43]. The pore size distribution of FMNs1.25 is given in Figure 7c. The distribution contains a sharp peak at 6 nm and a smaller peak at 22 nm. The average pore diameter was determined to be 8.32 nm. These data suggest that the fabricated catalysts had a high BET surface area and a mesoporous structure, which would result in the presence of a large number of active sites for the adsorbate. This, in turn, would promote the mass transfer of free radicals and hence dramatically improve the catalytic performance of the nanocomposites with respect to the organic pollutants present in wastewater [44,45].

The zeta potential and (b) diameter of FMNs1.25 were observed with the PH. As seen in Figure 8a, the Zeta potential of FMNs1.25 decreased with the rise of PH, the point of zero charge (PZC) of FMNs1.25 appeared between 3–5 of the initial PH of the reaction system, indicating the surface of FMNs1.25 was positively charged in solutions at PH below the PZC [46]. Therefore, the electrostatic attraction forces predominated at pH 3, leading to more organic pollutants adsorbing on the surface of catalysts and the COD$_{Cr}$ removal rate reached higher. The average diameter varied as a function of pH between 3 and 9, and the results are shown in Figure 8b. The highest diameter of FMNs1.25 was 1801.1 nm at the PH of 3, when the PH of the solution was 9, the diameter reached it lowest point at 649.5 nm. These results show that the dispersion of catalyst in solution was getting better with the increases of PH.
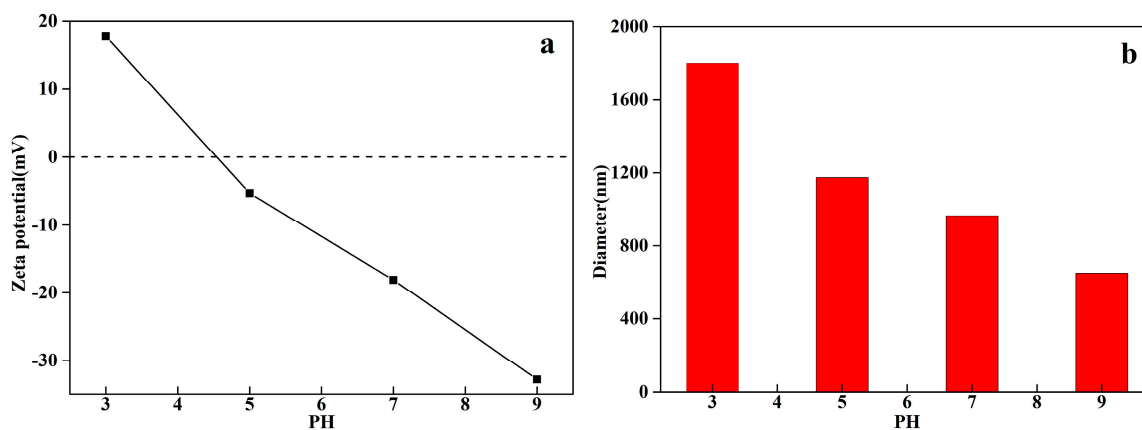

Figure 8. (**a**) Zeta potential and (**b**) diameter of FMNs1.25 as a function of PH.

3.2. Effects of Fe₃O₄/MnO₂ Nanocomposites on Treatment of Wastewater Through Heterogeneous Photocatalysis

A series of synthetic samples were applied to determine the COD_{Cr} removal efficiency, and the results are shown in Figure 9a. The areas of the curves before an elapsed time of 20 min represent the adsorption phase. It was obviously found that HFNs6 (pure Fe_3O_4) has lower COD_{Cr} removal efficiency compared with the Fe_3O_4/MnO_2 nanocomposites under the same tested conditions. Control experiments performed using FMNs1.25 in the absence of UV-vis light showed that, on its own, the absorption of FMNs1.25 was 25.03%, the COD_{Cr} of effluent after treatment was 89.96 mg/L. There was no appreciable degradation of COD_{Cr} without light irradiation. The observed decreases in the COD_{Cr} in the case of the FMNs were principally attributable to the catalytic generation of radicals and the adsorption of organic pollutants by Fe_3O_4/MnO_2 was limited. In contrast, after UV-vis light irradiation for 120 min, the maximal COD_{Cr} removal rates of FMNs0.5, FMNs1, FMNs1.25, FMNs1.5 and FMNs2 (reaction temperature of 25 °C, catalyst dosage: 1.75 g/L) were 43.58%, 45.57%, 56.58%, 50.66% and 47.83%, respectively. At the same time, the COD_{Cr} of effluent after treatment was 67.70 mg/L, 65.32 mg/L, 52.10 mg/L, 59.21 mg/L and 62.60 mg/L, respectively. The best COD_{Cr} removal rates (56.58%) were achieved by FMNs1.25, as indicated by the decreased COD_{Cr} concentrations from 120 mg/L to 52.10 mg/L, less than the prescribed level for discharge standard of water pollutants for pulp and paper industry in China. Previous studies have shown that under UV−vis light irradiation, the maximal degradation efficiency of methylene blue treated with a thin-layer MnO_2 nanosheet-coated Fe_3O_4 nanocomposite could reach 98.2% [27] and the maximum adsorption capacities of As(III) and As(V) were 76.73 mg/g and 120.50 mg/g, respectively [47]. This means the Fe_3O_4/MnO_2 nanocomposites have great potential, not only in the treatment of refractory industrial wastewater, but also in the treatment of heavy metal wastewater.
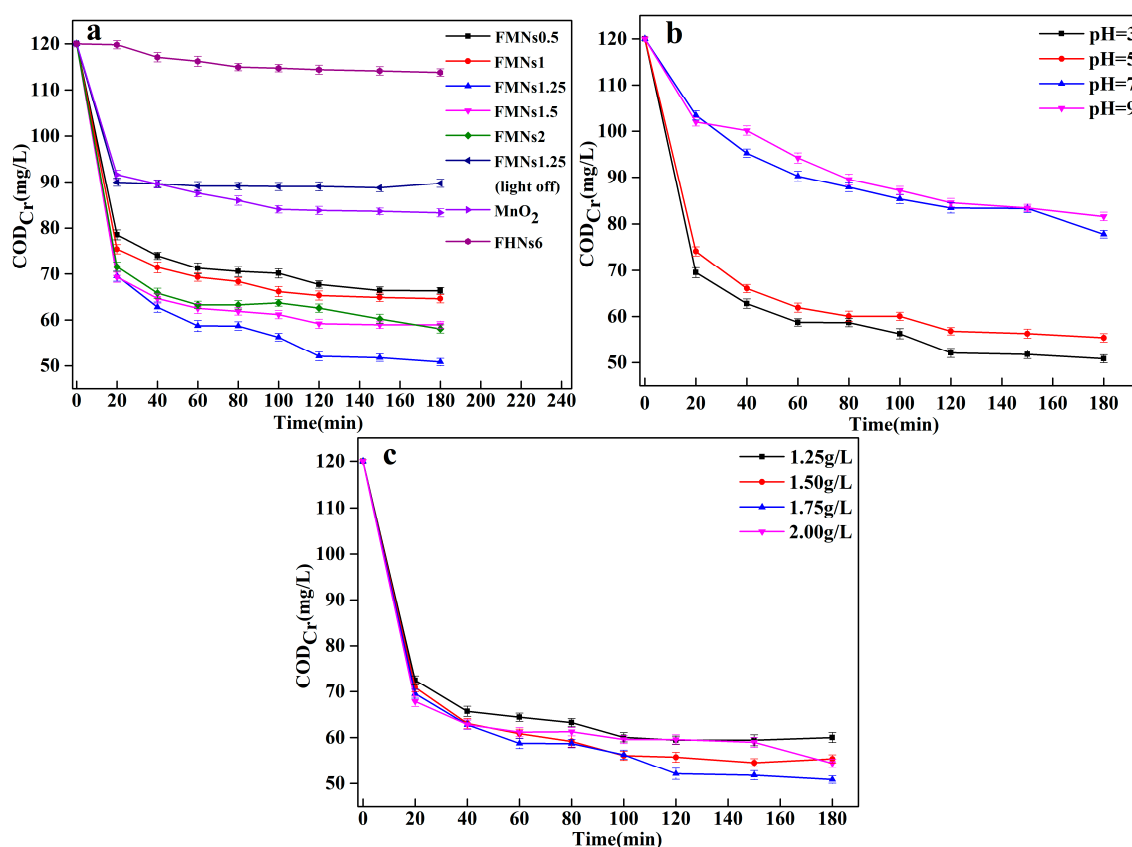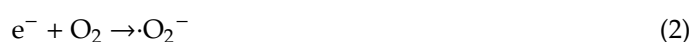

Figure 9. Effects of (**a**) FMNs sample, (**b**) initial PH, and (**c**) catalyst dosage on decrease in chemical oxygen demand (COD_{Cr}) of wastewater.

During the photocatalytic reaction, MnO_2 plays a more important role than Fe_3O_4 [48]. The BET surface area and BJH pore volume of the FMNs increase with the growth of the MnO_2 nanosheets. This, in turn, results in more active sites being present on the surfaces of the catalyst particles. Thus, the greater the amount of MnO_2 in the nanocomposites, the higher their catalytic activity will be (as seen in the cases of FMNs0.5 to FMNs1.25). However, when the MnO_2 loading amount was increased further (i.e., for FMNs1.25 to FMNs2), the BET surface area and BJH pore volume decreased, causing a decrease in the catalytic efficiency. Moreover, when MnO_2 and Fe_3O_4 were used individually as catalysts for the heterogeneous photocatalytic reaction, the COD_{Cr} of the effluent remained higher than the current discharge standard in both cases.

Next, the effects of the pH and catalyst dosage on the decrease in the COD_{Cr} were investigated using FMNs1.25 as the photocatalyst. Figure 9b showed that the rate of decrease in the COD_{Cr} reduced as the pH was increased from 3.0 to 9.0. The highest decrease in the COD_{Cr} (57.63%) was achieved at a pH 3, the COD_{Cr} of treated wastewater was 50.84 mg/L. Further, the COD_{Cr} of effluent after treatment was 77.78 mg/L at a pH of 7 and 81.60 mg/L at a pH of 9. Hence, the efficiency of the catalytic reaction was significantly affected by the initial pH of the treated wastewater. As can be seen from Figure 8b, during the first 20 min, the adsorption capacity under acidic conditions (pH values of 3–5) was larger than that under alkaline conditions (pH values of 7–9). These results agreed with Zhang's analysis [27], in that at acidic conditions, the surface of MnO_2 nanosheet-coated Fe_3O_4 nanocomposite is positively charged, and then ●OH production is accelerated. ●OH production is greatly advantageous for the photocatalytic degradation of MB. The reactions involved in the above-described process are as follow [49]:

$$e^- + O_2 \rightarrow \cdot O_2^- \tag{2}$$

$$e^- + H^+ + O_2^- \rightarrow HO_2^- \tag{3}$$

$$HO_2^- + H^+ \rightarrow H_2O_2 \tag{4}$$

$$O_2^- + H_2O \rightarrow HO_2^- + OH \tag{5}$$

The lower pH of reaction system, the higher concentration of H^+ ions in the solution, causing the surfaces of the solid-phase catalyst particles to be positively charged. As a result, a greater number of the photogenerated electrons in the system migrate to the surfaces of the catalyst particles. This results in the combination of the electrons and the O_2 that is adsorbed on the catalyst surfaces, leading to the generation of H_2O_2, this is consistent with Equations (2)–(4). Eventually, more ·OH is generated: Equation (5) represents the reaction process, resulting in an improvement in the efficiency of the catalytic reaction [49–51].

Thus, a pH of 3 was taken to be the optimal pH for the subsequent experiments to explore the effect of catalyst dosage on COD_{Cr} removal. Figure 9c shows the effects of the catalyst dosage on the rate of decrease in the wastewater COD_{Cr}. When the catalyst dosage was increased from 1.25 g/L to 1.75 g/L, the decrease in the COD_{Cr} removal rate of wastewater increased from 49.97% to 57.63%. Further, when the catalyst dosage was increased to 2 g/L, the COD_{Cr} of the wastewater decreased by 54.67%. The particle size of the synthesized catalysts was small and the particles were well dispersed in the wastewater, resulting in an increase in the turbidity for the solution. Hence, some of the incident light was scattered and did not participate in the photocatalytic reaction. This adversely affected the catalytic efficiency [52,53].

From the above results, the as-synthesized catalyst shows high efficiency in the advanced treatment of wastewater from the pulp and paper mill. Moreover, it has been proved that a magnetically recyclable thin-layer MnO_2 nanosheet-coated Fe_3O_4 nanocomposite performs well in the simulated dye wastewater [27]. In result, the Fe_3O_4/MnO_2 nanocomposites in this study have great potential for the advanced treatment of biotreated papermaking effluent, dye wastewater and other refractory organic wastewater.

3.3. Kinetics of Heterogeneous Photocatalytic Reaction

The kinetics of the heterogeneous photocatalytic reaction were also studied. The software Origin 9.0 was used to fit the data corresponding to the relationship between the COD_{Cr} decrease rate and the reaction time. The reaction for the measurements was performed under optimized conditions, which were as follows: A reaction temperature of 25 °C, contact time of 180 min, with the following catalyst used: FMNs1.25, with an initial pH of 3, and a catalyst dosage of 1.75 g/L. Figure 10a,b show the pseudo-first-order-kinetics and pseudo-second-order-kinetics models obtained after multiple fittings. The fitting equation for the pseudo-first-order-kinetics model is $Y = 0.24539 + (8.06311 \times 10^{-4})\,X$, with the pseudo-first-order-kinetics rate constant being 8.06311×10^{-4} and $R^2 = 0.87718$. In addition, the fitting equation for the pseudo-second-order-kinetics model is $Y = 0.21099 + 0.00175X - (4.75151 \times 10^{-6})\,X^2$, with the pseudo-second-order-kinetics rate constant being -4.75151×10^{-6} and $R^2 = 0.9506$. In the figures, the *y*-axis represents $\ln(C_0/C_t)$ while the *x*-axis represents the reaction time (min). These results indicated that the catalytic reaction was primarily driven by pseudo-second-order kinetics.
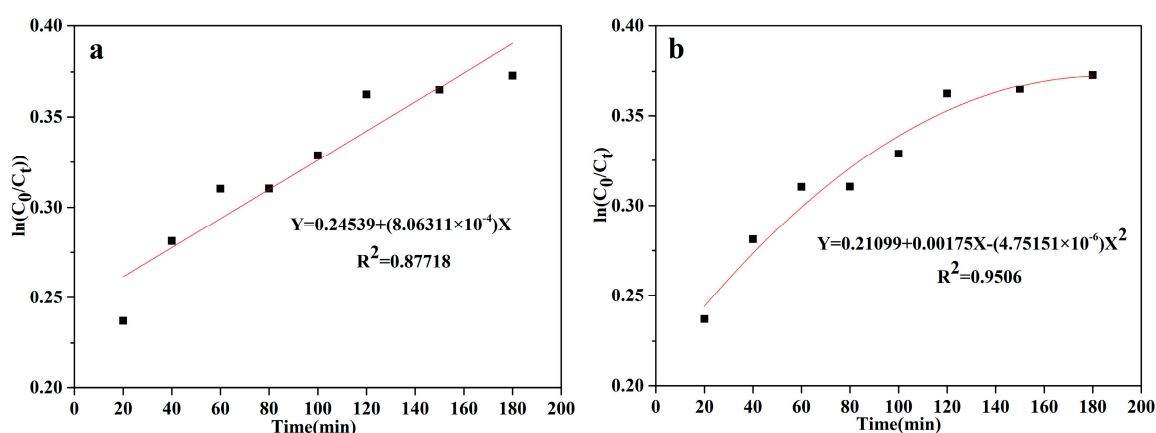

Figure 10. Fitted curves for (**a**) pseudo-first-order kinetics and (**b**) pseudo-second-order kinetics for decrease in COD_{Cr} during heterogeneous photocatalysis reaction (optimized conditions: Initial COD_{Cr} of 120 mg/L, FMNs1.25 concentration of 1.75 g/L, contact time of 180 min, solution pH of 3, and temperature of 25 °C).

3.4. Recyclability of Fe_3O_4/MnO_2 Nanocomposites

With respect to heterogeneous photocatalytic reactions, the recyclability and reusability of the catalyst used are important parameters for evaluating its industrial applicability. The magnetic properties of the nanocomposites fabricated in this study had a significant effect on their reusability. As shown in Figure 11a, the saturation magnetization (MS) values of the HFNs6 and FMNs1.25 were 56.22 emu/g and 31.34 emu/g, respectively, when subjected to an external magnetic field. This allowed for solid-liquid separation within 30 s. The MS value of FMNs1.25 was lower than that of the HFNs6, owing to the presence of nonmagnetic MnO_2 nanosheets, which limited its magnetization [27,47]. However, in spite of having a lower MS value, FMNs1.25 could be readily separated from an aqueous solution at a low magnetic field gradient (Figure 11a).

Reusability tests were performed, again under optimized conditions: Reaction temperature of 25 °C, the COD_{Cr} of the wastewater of 120 mg/L, contact time of 180 min, catalyst used: FMNs1.25, initial pH of 3, and catalyst dosage of 1.75 g/L. After each reaction, the photocatalyst used was separated from the wastewater sample being treated using an external magnetic field, and the collected catalyst was washed three times with water and ethanol respectively and dried at 60 °C for 24 h before the next experiment. The COD_{Cr} of the wastewater as measured after each test is shown in Figure 11b. It can be seen that, with an increase in the number of reaction cycles, the COD_{Cr} of wastewater after reaction decreased gradually. After the 5th cycle, COD_{Cr} reduced from the initial value of 120 mg/L to

approximately 67 mg/L, which achieved 80% of the initial use effect. This confirmed that the catalyst exhibited good recyclability and reusability.
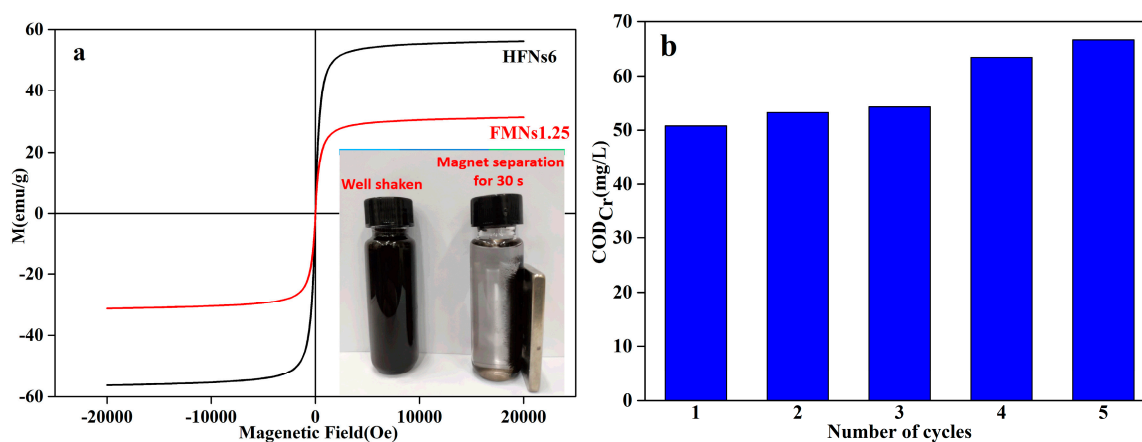

Figure 11. (**a**) Hysteresis loop of FMNs1.25 and (**b**) effect of number of reaction cycles on COD_{Cr} (optimized reaction conditions: Initial COD_{Cr} of 120 mg/L, FMNs1.25 concentration of 1.75 g/L, contact time of 180 min, solution pH of 3, and temperature of 25 °C).

3.5. Degradation of Organic Pollutants

3D-EEM spectroscopy is a useful technique of analyzing the chemical properties of the organic compounds present in the wastewater, which can be evaluated based on the position, shift, and intensity of the fluorescence peaks present in the obtained spectrum [54]. Figure 12a shows the 3D-EEM spectrum of an untreated wastewater sample while Figure 12b shows the 3D-EEM spectrum of the wastewater sample after the heterogeneous photocatalytic reaction. In this case too, the reaction was performed under optimized conditions: Reaction temperature of 25 °C, contact time of 180 min, with the following catalyst used: FMNs1.25, with an initial pH of 3, and a catalyst dosage of 1.75 g/L. As can be seen from Figure 12a, two distinct fluorescence peaks (A and B) were present in the spectrum of the untreated wastewater sample. Peak A was centered at E_x/E_m = 322 nm/435 nm and was the humic-related fluorescent peak in the visible region [55]. Furthermore, peak B was centered at E_x/E_m = 246 nm/425 nm and displayed the fulvic-related fluorescent peak in the visible region [56]. After the photocatalytic reaction under optimized conditions, the center of peak A changed to E_x/E_m = 318 nm/425 nm, while that of peak B moved to E_x/E_m = 246 nm/440 nm (see Figure 12b). Moreover, the changes in the peak intensities were used to determine the differences in the contents of the various fluorescent components of the wastewater sample before and after the photocatalytic reaction. The intensity of peak A in the untreated sample was 3.88×10^5 (a.u.) while that of peak B was 2.55×10^5 (a.u.). After the heterogeneous photocatalytic reaction, the intensity of peak A decreased to 1.78×10^5 (a.u.) while that of peak B decreased to 1.77×10^5 (a.u.), indicating that the removal rate of the humic-like substance was 54.12% while that of the fulvic-like substance was 30.60%. In conclusion, while the heterogeneous photocatalytic reaction could remove more of the humic-like material than the fulvic-like material present in the wastewater sample, both components were degraded to a high degree.
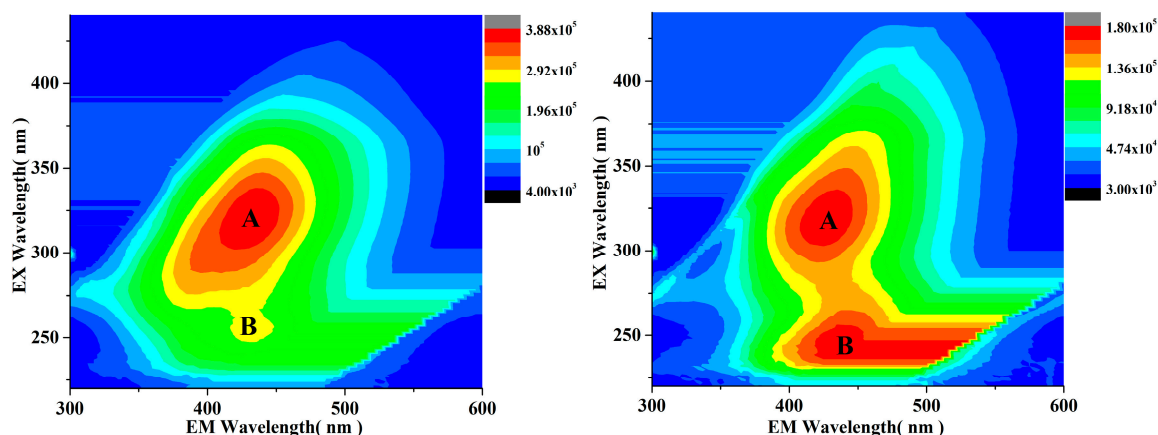
Figure 12. 3D-excitation-emission-matrix (3D-EEM) spectrum of (**a**) untreated wastewater and (**b**) wastewater after catalytic treatment (optimized conditions: Initial COD_{Cr} concentration of 120 mg/L, FMNs1.25 concentration of 1.75 g/L, contact time of 180 min, solution pH of 3, and a temperature of 25 °C).

4. Conclusions

To summarize, a series of magnetic, flower-like nanocomposites consisting of petal-like MnO_2 nanosheets coated on hollow Fe_3O_4 nanospheres were synthesized by way of a simple hydrothermal method and a subsequent coprecipitation process. Sample FMNs1.25, which was fabricated using a $KMnO_4/Fe_3O_4$ molar ratio of 1.25, exhibited higher photocatalytic activity than those of the other FMN nanocomposites as well as those of MnO_2 and Fe_3O_4; this was the case even under neutral reaction conditions. The use of FMNs1.25 reduced the COD_{Cr} in the effluent to less than the prescribed level for discharge standard of water pollutants for pulp and paper industry in China, indicating that it is highly suitable for the photocatalytic treatment of wastewater. Further, because of their magnetic properties, the fabricated nanocomposite catalysts also showed good recyclability and reusability when used repeatedly in the treatment reaction. Thus, the Fe_3O_4/MnO_2 nanocomposites fabricated have great potential for use as stable, efficient, environmentally friendly, and low-cost catalysts for the advanced treatment of refractory organic wastewater.

References

1. Barbosa, B.; Costa, J.; Fernando, A.L.; Papazoglou, A.L.; Papazoglou, E.G. Wastewater reuse for fiber crops cultivation as a strategy to mitigate desertification. *Ind. Crops Prod.* **2015**, *68*, 17–23. [CrossRef]
2. Shak, K.P.Y.; Wu, T.Y. Optimized use of alum together with unmodified Cassia obtusifolia seed gum as a coagulant aid in treatment of palm oil mill effluent under natural pH of wastewater. *Ind. Crops Prod.* **2015**, *76*, 1169–1178. [CrossRef]
3. Fang, F.; Yin, W.; Jiang, Y.; Ge, H.; Li, P.; Wu, J. Depth treatment of coal-chemical engineering wastewater by a cost-effective sequential heterogeneous Fenton and biodegradation process. *Environ. Sci. Pollut. Res. Int.* **2018**, *25*, 13118–13126. [CrossRef] [PubMed]
4. Peydayesh, M.; Mohammadi, T.; Bakhtiari, O. Effective Treatment of Dye Wastewater via Positively Charged TETA-MWCNT/PES Hybrid Nanofiltration Membranes. *Sep. Purif. Technol.* **2017**, *194*, 488–502. [CrossRef]

5. Boczkaj, G.; Fernandes, A. Wastewater treatment by means of advanced oxidation processes at basic pH conditions: A review. *Chem. Eng. J.* **2017**, *320*, 608–633. [CrossRef]

6. Sabatino, S.; Galia, A.; Saracco, G.; Scialdone, O. Development of an Electrochemical Process for the Simultaneous Treatment of Wastewater and the Conversion of Carbon Dioxide to Higher Value Products. *Chemelectrochem* **2017**, *4*, 150–159. [CrossRef]

7. Asghar, A.; Abdul Raman, A.A.; Wan Daud, W.M.A. Advanced oxidation processes for in-situ production of hydrogen peroxide/hydroxyl radical for textile wastewater treatment: A review. *J. Clean. Prod.* **2015**, *87*, 826–838. [CrossRef]

8. Hay, J.X.W.; Wu, T.Y.; Ng, B.J.; Juan, J.C.; Jahim, J.M. Reusing pulp and paper mill effluent as a bioresource to produce biohydrogen through ultrasonicated Rhodobacter sphaeroides. *Energy Convers. Manag.* **2016**, *113*, 273–280. [CrossRef]

9. Saif, Y.; Almansoori, A.; Elkamel, A. Wastewater Minimization in Pulp and Paper Industries through Energy-Efficient Reverse-Osmosis Membrane Processes. *Chem. Eng. Technol.* **2013**, *36*, 419–425. [CrossRef]

10. Gadipelly, C.; Pérez-González, A.; Yadav, G.D.; Ortiz, I.; Ibáñez, R.; Rathod, V.K. Pharmaceutical Industry Wastewater: Review of the Technologies for Water Treatment and Reuse. *Ind. Eng. Chem. Res.* **2014**, *53*, 11571–115592. [CrossRef]

11. Sarkar, S.; Ali, S.; Rehmann, L.; Nakhla, G.; Ray, M.B. Degradation of estrone in water and wastewater by various advanced oxidation processes. *J. Hazard. Mater.* **2014**, *278*, 16–24. [CrossRef] [PubMed]

12. Sun, W.L.; Qu, Y.Z.; Yu, Q.; Ni, J.R. Adsorption of organic pollutants from coking and papermaking wastewaters by bottom ash. *J. Hazard. Mater.* **2008**, *154*, 595–601. [CrossRef] [PubMed]

13. Lim, B.R.; Hu, H.Y.; Fujie, K. Biological Degradation and Chemical Oxidation Characteristics of Coke-Oven Wastewater. *Water Air Soil Pollut.* **2003**, *146*, 23–33. [CrossRef]

14. Gimeno, O.; García-Araya, J.F.; Beltrán, F.J.; Rivas, F.J.; Espejo, A. Removal of emerging contaminants from a primary effluent of municipal wastewater by means of sequential biological degradation-solar photocatalytic oxidation processes. *Chem. Eng. J.* **2016**, *290*, 12–20. [CrossRef]

15. Carbonaro, S.; Sugihara, M.N.; Strathmann, T.J. Continuous-flow photocatalytic treatment of pharmaceutical micropollutants: Activity, inhibition, and deactivation of TiO_2, photocatalysts in wastewater effluent. *Appl. Catal. B Environ* **2013**, *129*, 1–12. [CrossRef]

16. Márquez, G.; Gracia, R.; Eva, M.; Maldonado, M.I.; Alvarez, P.M. Integration of ozone and solar TiO_2-photocatalytic oxidation for the degradation of selected pharmaceutical compounds in water and wastewater. *Sep. Purif. Technol.* **2014**, *136*, 18–26. [CrossRef]

17. Liu, D.; Garcia, B.B.; Zhang, Q.; Guo, Q.; Zhang, Y.; Sepehri, S. Mesoporous Hydrous Manganese Dioxide Nanowall Arrays with Large Lithium Ion Energy Storage Capacities. *Adv. Funct. Mater.* **2009**, *19*, 1015–1023. [CrossRef]

18. Cheng, F.; Chen, J.; Gou, X.; Shen, P.W. High-Power Alkaline Zn–MnO_2 Batteries Using γ-MnO_2 Nanowires/Nanotubes and Electrolytic Zinc Powder. *Adv. Mater.* **2010**, *17*, 2753–2756. [CrossRef]

19. Dose, W.M.; Donne, S.W. Optimizing Heat Treatment Environment and Atmosphere of Electrolytic Manganese Dioxide for Primary Li/MnO_2 Batteries. *J. Power Sources* **2014**, *247*, 852–857. [CrossRef]

20. Wei, W.; Cui, X.; Chen, W.; Ivey, D.G. Manganese oxide-based materials as electrochemical supercapacitor electrodes. *Chem. Soc. Rev.* **2011**, *40*, 1697–1721. [CrossRef]

21. Yu, G.; Hu, L.; Liu, N.; Wang, H.; Vosgueritchian, M.; Yang, Y.; Cui, Y.; Bao, Z. Enhancing the Supercapacitor Performance of Graphene/MnO_2 Nanostructured Electrodes by Conductive Wrapping. *Nano Lett.* **2015**, *11*, 4438–4442. [CrossRef] [PubMed]

22. Wu, Z.S.; Ren, W.; Wang, D.W.; Li, F.; Liu, B.; Cheng, H.-M. High-Energy MnO_2 Nanowire/Graphene and Graphene Asymmetric Electrochemical Capacitors. *ACS Nano* **2010**, *4*, 5835–5842. [CrossRef] [PubMed]

23. Brimblecombe, R.; Koo, A.; Dismukes, G.C.; Swiegers, G.F.; Spiccia, L. Solar Driven Water Oxidation by a Bioinspired Manganese Molecular Catalyst. *J. Am. Chem. Soc.* **2010**, *132*, 2892–2894. [CrossRef] [PubMed]

24. Shafi, P.M.; Dhanabal, R.; Chithambararaj, A.; Velmathi, S.; Bose, A.C. α-MnO_2/h-MoO_3 Hybrid Material for High Performance Supercapacitor Electrode and Photocatalyst. *ACS Sustain. Chem. Eng.* **2017**, *5*, 4757–4770. [CrossRef]

25. Shang, K.; Ai, S.; Ma, Q.; Tang, T.; Yin, H.; Han, H. Effective photocatalytic disinfection of E. coli and S. aureus using polythiophene/MnO_2 nanocomposite photocatalyst under solar light irradiation. *Desalination* **2011**, *278*, 173–178. [CrossRef]

26. Pradhan, A.C.; Nanda, B.; Parida, K.M.; Rao, G.R. Fabrication of the Mesoporous Fe@MnO$_2$NPs-MCM-41 Nanocomposite: An Efficient Photocatalyst for Rapid Degradation of Phenolic Compounds. *J. Phys. Chem. C* **2015**, *119*, 14145–14159. [CrossRef]

27. Zhang, L.; Lian, J.; Wu, L.; Duan, Z.; Jiang, J.; Zhao, L. Synthesis of a thin-layer MnO$_2$ nanosheet-coated Fe$_3$O$_4$ nanocomposite as a magnetically separable photocatalyst. *Langmuir* **2014**, *30*, 7006–7013. [CrossRef]

28. Xia, P.; Zhu, B.; Cheng, B.; Yu, J.; Xu, J. 2D/2D g-C$_3$N$_4$/MnO$_2$ nanocomposite as a direct Z-scheme photocatalyst for enhanced photocatalytic activity. *ACS Sustain. Chem. Eng.* **2018**, *6*, 965–973. [CrossRef]

29. Yang, Z.; Yang, Y.; Zhu, X.; Chen, G.; Zhang, W. An Outward Coating Route to CuO/MnO$_2$ Nanorod Array Films and Their Efficient Catalytic Oxidation of Acid Fuchsin Dye. *Ind. Eng. Chem. Res.* **2014**, *53*, 9608–9615. [CrossRef]

30. Nawaz, F.; Xie, Y.; Cao, H.; Xiao, J.; Wang, Y.; Zhang, X.; Li, M.; Duan, F. Catalytic ozonation of 4-nitrophenol over an mesoporous α-MnO$_2$ with resistance to leaching. *Catal. Today* **2015**, *258*, 595–601. [CrossRef]

31. Wang, X.; Dou, L.; Yang, L.; Yuc, J.; Ding, B. Hierarchical structured MnO$_2$@SiO$_2$ nanofibrous membranes with superb flexibility and enhanced catalytic performance. *J. Hazard. Mater.* **2017**, *324*, 203–212. [CrossRef] [PubMed]

32. Zhao, Z.; Liu, J.; Cui, F.; Fenga, H.; Zhanga, L. One pot synthesis of tunable Fe$_3$O$_4$-MnO$_2$ core–shell nanoplates and their applications for water purification. *J. Mater. Chem.* **2012**, *22*, 9052–9057. [CrossRef]

33. Shokouhimehr, M.; Piao, Y.; Kim, J.; Jang, Y.; Hyeon, T. A magnetically recyclable nanocomposite catalyst for olefin epoxidation. *Angew. Chem.* **2007**, *46*, 7039–7043. [CrossRef] [PubMed]

34. Zhou, L.; Yuan, J.; Wei, Y. Core–shell structural iron oxide hybrid nanoparticles: From controlled synthesis to biomedical applications. *J. Mater. Chem.* **2011**, *21*, 2823–2840. [CrossRef]

35. Mishra, K.; Basavegowda, N.; Lee, Y.R. Biosynthesis of Fe, Pd, and Fe-Pd bimetallic nanoparticles and their application as recyclable catalysts for [3+2] cycloaddition reaction: A comparative approach. *Catal. Sci. Technol.* **2015**, *5*, 2612–2621. [CrossRef]

36. Zhai, Y.; Zhai, J.; Zhou, M.; Dong, S. Ordered magnetic core–manganese oxide shell nanostructures and their application in water treatment. *J. Mater. Chem.* **2009**, *19*, 7030–7035. [CrossRef]

37. Ma, Z.; Guan, Y.; Liu, H. Synthesis and characterization of Micron-Sized mono disperse super paramagnetic polymer particles with amino groups. *J. Polym. Sci. Pol. Chem.* **2005**, *43*, 3433–3439. [CrossRef]

38. Xu, M.W.; Zhao, D.D.; Bao, S.J.; Li, H.L. Mesoporous amorphous MnO$_2$ as electrode material for supercapacitor. *J. Solid State Electrochem.* **2007**, *11*, 1101–1107. [CrossRef]

39. Wang, N.H.; Lo, S.L. Preparation, characterization and adsorption performance of cetyltrimethylammonium modified birnessite. *Appl. Surf. Sci.* **2014**, *299*, 123–130. [CrossRef]

40. Yang, X.; Makita, Y.; Liu, Z.H.; Sakane, K.; Ooi, K. Structural Characterization of Self-Assembled MnO$_2$ Nanosheets from Birnessite Manganese Oxide Single Crystals. *Chem. Mater.* **2004**, *16*, 5581–5588. [CrossRef]

41. Brunold, T.C.; Gamelin, D.R.; Stemmler, T.L.; Mandal, S.K.; Armstrong, W.H.; Penner-Hahn, J.E.; Solomon, E.I. Spectroscopic Studies of Oxidized Manganese Catalase and μ-Oxo-Bridged Dimanganese(III) Model Complexes: Electronic Structure of the Active Site and Its Relation to Catalysis. *J. Am. Chem. Soc.* **1998**, *120*, 8724–8738. [CrossRef]

42. Jana, S.; Basu, S.; Pande, S.; Ghosh, S.K.; Pal, T. Electrochemical properties and hydrogen storage mechanism of perovskite-type oxide LaFeO$_3$ as a negative electrode for Ni/MH batteries. *J. Phys. Chem. C* **2007**, *111*, 16272–16277. [CrossRef]

43. Freeman, J.J.; Mcleod, A.I. Nitrogen BET surface area measurement as a fingerprint method for the estimation of pore volume in active carbons. *Fuel* **1983**, *62*, 1090–1091. [CrossRef]

44. Na, K.; Jo, C.; Kim, J.; Ahn, W.-S.; Ryoo, R. MFI Titanosilicate Nanosheets with Single-Unit-Cell Thickness as an Oxidation Catalyst Using Peroxides. *ACS Catal.* **2011**, *1*, 901–907. [CrossRef]

45. Huang, R.; Liu, Y.; Chen, Z.; Pan, D.; Li, Z.; Wu, M.; Shek, C.-H.; Wu, C.M.L.; Lai, J.K.L. Fe-Species-Loaded Mesoporous MnO$_2$ Superstructural Requirements for Enhanced Catalysis. *ACS Appl. Mater. Interfaces* **2015**, *7*, 3949–3959. [CrossRef] [PubMed]

46. Hu, C.; Sun, J.; Wang, S. Enhanced efficiency in HA removal by electrocoagulation through optimizing flocs properties: Role of current density and pH. *Sep. Purif. Technol.* **2017**, *175*, 248–254. [CrossRef]

47. Wen, Z.; Zhang, Y.; Wang, Y.; Li, L.; Chen, R. Redox transformation of arsenic by magnetic thin-film MnO$_2$ nanosheet-coated flowerlike Fe$_3$O$_4$ nanocomposites. *Chem. Eng. J.* **2017**, *312*, 39–49. [CrossRef]

48. Saputra, E.; Muhammad, S.; Sun, H.; Ang, H.-M.; Tadé, M.O.; Wang, S. A comparative study of spinel structured Mn_3O_4, Co_3O_4 and Fe_3O_4 nanoparticles in catalytic oxidation of phenolic contaminants in aqueous solutions. *J. Colloid Interface Sci.* **2013**, *407*, 467–473. [CrossRef]

49. Kuo, C.Y. Prevenient dye-degradation mechanisms using UV/TiO_2/carbon nanotubes process. *J. Hazard. Mater.* **2009**, *163*, 239–244. [CrossRef]

50. Yu, Y.; Yu, J.C.; Yu, J.G.; Kwok, Y.-C.; Che, Y.-K.; Zhao, J.-C.; Ding, L.; Ge, W.-K.; Wong, P.-K. Enhancement of photocatalytic activity of mesoporous TiO_2 by using carbon nanotubes. *Appl. Catal. A Gen.* **2005**, *289*, 186–196. [CrossRef]

51. Liu, J.; Bai, H.; Wang, Y.; Liu, Z.; Zhang, X.; Sun, D.D. Self-Assembling TiO_2 Nanorods on Large Graphene Oxide Sheets at a Two-Phase Interface and Their Anti-Recombination in Photocatalytic Applications. *Adv. Funct. Mater.* **2010**, *20*, 4175–4181. [CrossRef]

52. Muruganandham, M.; Swaminathan, M. Photochemical oxidation of reactive azo dye with UV–H_2O_2 process. *Dyes Pigments* **2004**, *62*, 269–275. [CrossRef]

53. Iurascu, B.; Siminiceanu, I.; Vione, D.; Vicente, M.A.; Gild, A. Phenol degradation in water through a heterogeneous photo-Fenton process catalyzed by Fe-treated laponite. *Water Res.* **2009**, *43*, 1313–1322. [CrossRef] [PubMed]

54. Jin, P.; Jin, X.; Bjerkelund, V.A.; Østerhus, S.W.; Wang, X.C.; Yang, L. A study on the reactivity characteristics of dissolved effluent organic matter (EfOM) from municipal wastewater treatment plant during ozonation. *Water Res.* **2016**, *88*, 643–652. [CrossRef] [PubMed]

55. Zhao, H.; Chen, D.; Li, Y.; Cai, B. Overexpression, purification and characterization of a new salicylate hydroxylase from naphthalene-degrading Pseudomonas sp. strain ND6. *Microbiol. Res.* **2005**, *160*, 307–313. [CrossRef] [PubMed]

56. Matthews, B.J.H.; Jones, A.C.; Theodorou, N.K.; Tudhope, A.W. Excitation-emission-matrix fluorescence spectroscopy applied to humic acid bands in coral reefs. *Mar. Chem.* **1996**, *55*, 317–332. [CrossRef]